# Topology optimization of 3D shell structures with porous infill

**Clausen, Anders; Andreassen, Erik; Sigmund, Ole**

*Published in:*
Acta Mechanica Sinica

*Link to article, DOI:*
10.1007/s10409-017-0679-2

*Publication date:*
2017

# Topology optimization of 3D shell structures with porous infill

Anders Clausen[a], Erik Andreassen[a], Ole Sigmund[a,*]

[a]*Department of Mechanical Engineering, Solid Mechanics, Technical University of Denmark, Nils Koppels Alle, B. 404, DK-2800 Lyngby, Denmark*

**Abstract**

This paper presents a 3D topology optimization approach for designing shell structures with a porous or void interior. It is shown that the resulting structures are significantly more robust towards load perturbations than completely solid structures optimized under the same conditions. The study indicates that the potential benefit of using porous structures is higher for lower total volume fractions. Compared to earlier work dealing with 2D topology optimization, we found several new effects in 3D problems. Most notably, the opportunity for designing closed shells significantly improves the performance of porous structures due to the sandwich effect. Furthermore, the paper introduces improved filter boundary conditions to ensure a completely uniform coating thickness at the design domain boundary.

*Keywords:* Topology optimization, Coating, Shell structure, Two-step filtering

## 1. Introduction

This paper presents a design methodology for creating 3D porous shell structures, that is, structures consisting of a porous base structure with a solid shell of uniform thickness at all external interfaces. The work extends the so-called coating approach to topology optimization originally introduced for 2D problems by Clausen et al. (2015). The approach is suitable for two types of problems: (1) modeling of coated structures, e.g. metallic coating of polymers (Schaedler et al., 2011; Møller and Nielsen, 2013) which is used in industry to combine the benefits of the two materials regarding performance, cost and manufacturability, or (2) the opportunity of creating shell structures with porous infill, an example of a unique additive manufacturing capability which is typically not taken into account in automated design processes.

Shell structures with a light, porous infill can obtain a high bending stiffness-to-weight ratio by separating the solid shells away from center axes of local bars making up the optimized structure, a principle similar to that employed for sandwich or I-beam structures. Figure 1 illustrates how this effect may provide robustness towards uncertain loading conditions. The figure compares two cylindrical cantilever beams compressed by a concentrated load. One beam is fully solid with radius $r_0$ (Figure 1a), the other is composed of a solid shell with porous interior (Figure 1b), having an outer radius of $r_{\text{out}} = 2r_0$. The porous infill is isotropic, with the relation between density and stiffness following the Hashin-Shtrikman upper bound (described in detail

*Corresponding author
*Email address:* sigmund@mek.dtu.dk (Ole Sigmund)

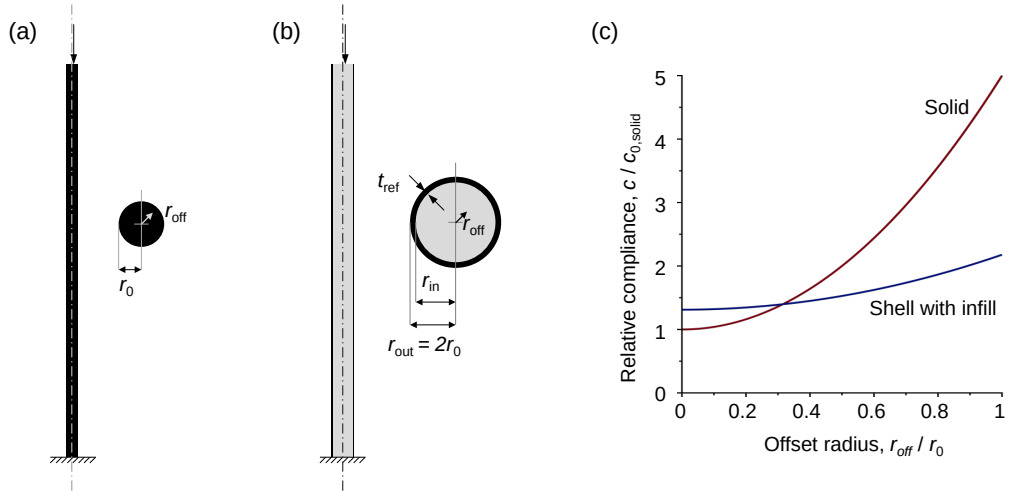


Figure 1: Variation in compliance with loading offset for solid beam vs. shell beam with porous infill. (a) Solid cylindrical beam with cross-section of radius $r_0$.(b) Porous cylindrical beam with outer cross-section radius $r_{out} = 2r_0$ and a shell thickness of $t_{\text{ref}} = r_0/8$. (c) Compliance curves for the two beams when varying the loading offset distance, $r_{\text{off}}$.

below). The density of the infill is chosen such that the total mass of the two beams is identical. The load is applied axially, but offset by a distance $r_{\text{off}}$ from the beams' center axes. Figure 1c compares the compliance of the two beams for varying loading offset distance. At zero offset, the porous beam has approximately 30 % higher compliance. However, for a non-zero offset, the resulting bending deformation adds a contribution to the compliance, which significantly increases the compliance of the solid beam. Already from an offset distance of around $r_{\text{off}} = 0.3r_0$ the compliance of the solid beam exceeds that of the porous one, and at $r_{\text{off}} = r_0$ it is 2.3 times higher. The lower variation in performance and thereby higher robustness of the porous beam is evident. Furthermore, the buckling load of the porous beam is 4.6 times higher than that of the solid beam, a topic which was already investigated in detail by Clausen et al. (2016), who showed an experimentally validated example of a 2D optimized, porous structure which possessed a buckling load that was nearly five times higher than that of a thinner and fully solid structure with the same mass.

In this work, we will further explore the robustness to various loading conditions for topology optimized, porous 3D shell structures.

The coating approach, which this work builds on, may be characterized as an interface problem. Other works treating 2D interface problems in a topology optimization context include Vermaak et al. (2014) who suggested a formulation for introducing a transition zone of graded properties in multi-phase materials, and Donoso and Sigmund (2016) who imposed a null-polarity phase in piezo modal transducers.

In this work the method for modeling 2D structures with porous infill Clausen et al. (2016) is extended to 3D by adapting the implementation to a large-scale, parallelized computational framework (Aage et al., 2015). The addition of a third dimension changes the design opportunities fundamentally, since pure shell structures with vanishing base structure stiffness still have significant load carrying capacity in 3D. For instance, consider Figure 2. The bending stiffness and buckling load for two parallel 2D bars separated by a core of vanishing stiffness (Figure 2a)

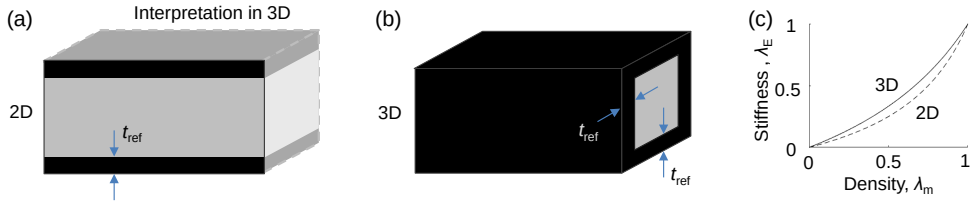


Figure 2: Model of coated feature. (a) 2D coated feature and its 3D interpretation obtained by extrusion. (b) 3D coated feature. (c) Hashin-Shtrikman upper bound on stiffness for isotropic materials in 2D versus 3D.

are very low, as opposed to the properties of a hollow 3D shell structure (Figure 2b). New effects can therefore be observed when studying the 3D problem as compared to the previous 2D works.

We restrict the present work to structures for which the porous filling is isotropic and made of the same material as the coating (and void). In this case, the infill density, $\lambda_m$, and stiffness, $\lambda_E$, expressed as ratios of the fully solid material, should satisfy the Hashin-Shtrikman bounds on stiffness in order to be physically meaningful (Hashin and Shtrikman, 1963). Figure 2c compares the bounds for 2D plane stress versus 3D. Assuming a base material Poisson's ratio of 1/3, the two curves are given by the following simple expressions:

$$\begin{aligned} \lambda_E &= \frac{\lambda_m}{3-2\lambda_m}, \qquad \text{(2D)} \\ \lambda_E &= \frac{\lambda_m}{2-\lambda_m}, \qquad \text{(3D)} \end{aligned} \tag{1}$$

The simplified 2D relation is derived e.g. by Torquato et al. (1998). The simplified 3D relation is obtained using the usual relation

$$E = \frac{9KG}{3K+G}, \tag{2}$$

where $K$ and $G$ are the bulk and shear moduli of the fully solid material, respectively, but substituting $K$ and $G$ with the upper bound expressions provided by Hashin and Shtrikman (1963) for the effective bulk modulus, $K^*$, and effective shear modulus, $G^*$:

$$K^* \leq \frac{4GK\lambda_m}{4G+3K(1-\lambda_m)}, \tag{3}$$

$$G^* \leq G + \frac{1-\lambda_m}{\frac{6}{5G}\frac{(K+2G)\lambda_m}{(3K+4G)} - \frac{1}{G}}. \tag{4}$$

This approach assumes that the maximum bulk and shear moduli can be realized simultaneously. Equations 3 and 4 are here shown in the form used by Andreassen et al. (2014).

Due to the sublinear relation between density and stiffness for the porous material, a fully solid structure should always have a lower compliance compared to a structure incorporating porous, isotropic infill, if the length scales of the two structures are comparable. However, as illustrated by the example in Figure 1, a porous interior provides other structural advantages and is therefore relevant for more complex design goals than pure compliance.

An advantage of designing porous shell structures with the proposed coating approach is that above structural benefits are implicitly ensured and not explicitly included in the optimization. It is therefore a computationally cheap and simple way of ensuring improved structural robustness. An alternative but less efficient way of implicitly ensuring a higher buckling load is to restrict the structure from generating thin features, e.g. by using a larger filter radius. However, this approach does not allow the forming of porous, coated elements and should perform worse than the suggested coating approach.

The remainder of the paper is structured as follows: First the problem formulation is presented in Section 2, including the optimization problem, the main points of the coating approach and their adaption to the 3D case. Improved filter boundary conditions are presented in Section 3. We employ the domain extension approach suggested by Clausen and Andreassen (2017). In Section 4 numerical results are presented and discussed in relation to our initial hypothesis. The results are further discussed in Section 5 and the work is concluded in Section 6.

## 2. Problem formulation

This section presents the problem formulation, with focus on the two-step filter process and the particular material model employed in the coating approach. The interior of a coated structure is referred to as the base structure, as opposed to the coating which must be applied with a uniform thickness at all interfaces between base structure and void.

### *2.1. Optimization problem*

The considered optimization problem is a standard minimum compliance problem with a constraint on the volume. The discretized problem is defined in the following way:

$$\begin{aligned} \min_{\boldsymbol{\mu}}: \quad & c(\boldsymbol{\mu}) = \mathbf{U}^{\mathbf{T}}\mathbf{K}(\boldsymbol{\mu})\mathbf{U} \\ \text{subject to:} \quad & \mathbf{K}(\boldsymbol{\mu})\mathbf{U} = \mathbf{F}, \\ & g(\boldsymbol{\mu}) = V(\boldsymbol{\mu})/V^* - 1 \leq 0, \\ & 0 \leq \mu_e \leq 1, \quad \forall e, \end{aligned} \tag{5}$$

where $\boldsymbol{\mu}$ is the vector of design variables, $c$ is the compliance, $\mathbf{U}$ and $\mathbf{F}$ are the global displacement and force vectors, respectively, $\mathbf{K}$ is the global stiffness matrix, $g$ is the volume constraint, $V$ is the material volume and $V^*$ is the maximum allowed volume. A more precise definition of the global stiffness matrix, $\mathbf{K}$, and its dependence on $\boldsymbol{\mu}$, is presented in relation to the coating interpolation function in Section 2.3.

### *2.2. Two-step filtering approach*

The coating approach uses a single underlying design variable field. Two smoothing steps with subsequent projections define the geometry of the base structure and the coating. The scheme is illustrated in Figure 3, with the starting point being the field of mathematical design variables, $\mu$. The two filtering steps may be seen as two separate operations. The first step, going from $\mu$ to $\varphi = \bar{\tilde{\mu}}$ is identical to a standard formulation with a density filter of radius $R_1$ followed by a projection of sharpness $\beta$ at the threshold $\eta$, as reviewed in Sigmund (2007). This step ensures a nearly black-and-white base structure in the field, $\varphi$. The second step models

the coating by using the spatial gradients of the base structure. First the base structure field is smoothed using the radius $R_2$, to obtain $\hat{\varphi}$ ($R_2$ controls the thickness of the coating). Then the gradient norm of this field is normalized and subsequently projected using a sharpness $\beta_g$ at the threshold $\eta_g$, to obtain the coating field, $\overline{\|\nabla\hat{\varphi}\|}_\alpha$. The index $\alpha$ refers to the normalization. These fields enter in the density and stiffness interpolation function as described in Section 2.3.

*2.2.1. Smoothing and projection*

The two-step filtering procedure involves several smoothing and projection operations. The smoothing operation is performed using a density filter—in this work a PDE-based filter (Lazarov and Sigmund, 2011). This filter smooths the design by solving a second order partial differential equation:

$$-\left(\frac{R}{2\sqrt{3}}\right)^2\nabla^2\hat{\mu}+\hat{\mu}=\mu. \tag{6}$$

The filter radius, $R$, corresponds to the radius used in the standard, image-based filtering techniques. For the coating approach, the filter boundary conditions (BCs) must be chosen appropriately in order for the coating thickness to be applied uniformly in the entire domain (see Section 3).

A projection scheme (Guest et al., 2004; Sigmund, 2007) is employed in order to ensure a sharp interface at the base structure as well as a crisply defined coating. A version which permits an intermediate threshold value is employed (Xu et al., 2010; Wang et al., 2011):

$$\bar{\hat{\mu}}=\frac{\tanh(\beta\eta)+\tanh(\beta(\hat{\mu}-\eta))}{\tanh(\beta\eta)+\tanh(\beta(1-\eta))}, \tag{7}$$

where $\eta\in[0;1]$ is the threshold value and $\beta$ the projection sharpness. In this work, $\beta$ is initially chosen as 8, then gradually increased to 64 by multiplying it with 1.2 every 50 iterations or at convergence (the smallest change in any design variable is below 1%).

*2.2.2. Gradient normalization and coating thickness*

The maximum possible gradient norm in the second, filtered density field will occur at the interface between a fully solid and a completely void half space. Since the norm is computed for the smoothed field, its value is bounded. As was shown in Clausen et al. (2015), the maximum gradient norm value can be calculated analytically by assuming $\eta=0.5$ and $\beta\to\infty$. Conveniently, the use of a PDE-filter permits to reduce the problem to the corresponding 1D problem, that is, a Heaviside step function, $\varphi_H(x)=H(x)$. The argument used for the 2D case is completely analogous in 3D and is not repeated here. It suffices to state that the maximum value is $\|\nabla\hat{\varphi}_H\|_{max}=\sqrt{3}/R_2$, implying a normalization factor $\alpha_{3D}=\alpha_{2D}=R_2/\sqrt{3}$. The reader is referred to Clausen et al. (2015) for details.

Another useful result based on the analytical maximum gradient norm value is that also an analytical relation can be established between the uniform coating thickness and the filter radius $R_2$ of the second smoothing. In other words, the coating thickness can be prescribed through the value of $R_2$:

$$R_2=\frac{\sqrt{3}}{\ln(2)}t_{\text{ref}}\approx 2.5t_{\text{ref}}. \tag{8}$$

The reader is again referred to (Clausen et al., 2015) for details on the derivation. Remark, that this relation only holds if the base structure is sufficiently wide compared to the coating thickness. This point will be discussed in more detail in Section 2.4.

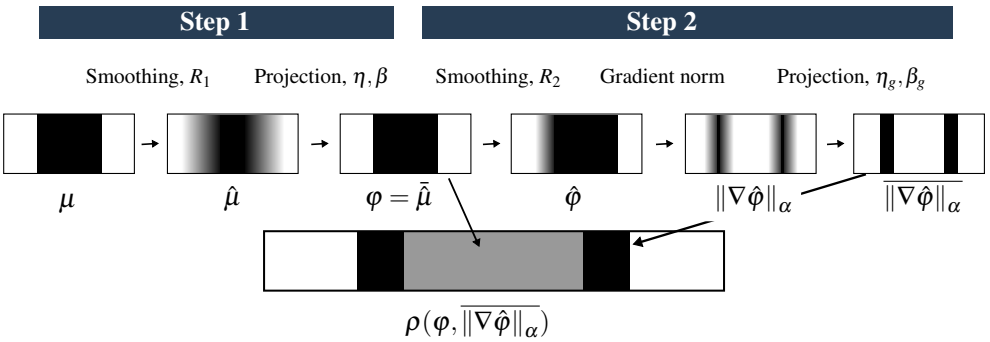


Figure 3: Two-step filtering process. $\rho$ represents the interpolation of the physical density.

### *2.3. Interpolation function*

The coating interpolation function includes spatial gradients. As opposed to the standard SIMP approach, the physical density is not simply a filtered/projected version of the design variable field, but itself an interpolation involving both the projected design variable field, $\varphi$, and its spatial gradient field through the variable $\overline{\|\nabla\hat{\varphi}\|_\alpha}$.

For simplicity the mass density of the coating material is assumed to be $m^0 = 1$. The materials are assumed to be isotropic with a Poisson's ratio, $\nu^0 = 1/3$, independent of interpolation density. The physical density, $\rho$, and stiffness, $E$, are defined as:

$$\rho(\varphi, \overline{\|\nabla\hat{\varphi}\|_\alpha}) = \lambda_m\varphi + (1 - \lambda_m\varphi)\overline{\|\nabla\hat{\varphi}\|_\alpha}, \tag{9}$$

$$E(\varphi, \overline{\|\nabla\hat{\varphi}\|_\alpha}) = E^0\left[\lambda_E\varphi^p + (1 - \lambda_E\varphi^p)(\overline{\|\nabla\hat{\varphi}\|_\alpha})^{p_g}\right]. \tag{10}$$

We use the penalization parameter $p = 3$ for the base structure, while we use $p_g = 1$ for the coating in order not to penalize low gradients at early design iterations.

Away from the interface, that is where $\overline{\|\nabla\hat{\varphi}\|_\alpha} \approx 0$, the expressions reduce to the SIMP-like $\rho = \lambda_m\varphi$ and $E = E^0\lambda_E\varphi^p$ material model. On the other hand, at the interface where $\overline{\|\nabla\hat{\varphi}\|_\alpha} \approx 1$ the physical density and stiffness approach 1 and $E^0$, respectively. As a consequence, base material is enforced where the design field equals 1 and has a low gradient, while coating material is enforced where the spatial gradient is large. In addition to the intuitive sketch presented in relation to the two-step filter in Figure 3, a graphical representation of the interpolation may be seen in the subsequent section where the relation between feature size and coating thickness is discussed.

Based on this interpolation function, the assembly of the global stiffness matrix, $\mathbf{K}$, can be expressed as:

$$\mathbf{K}(\boldsymbol{\mu}) = \sum_e \mathbf{k}_e(\boldsymbol{\mu}) = \sum_e E_e(\varphi_e(\boldsymbol{\mu}), \overline{\|\nabla\hat{\varphi}_e(\boldsymbol{\mu})\|_\alpha})\mathbf{k}_e^0, \tag{11}$$

where $\mathbf{k}_e$ is the element stiffness matrix, $\mathbf{k}_e^0$ is the element stiffness matrix for an element with unit Young's modulus, and summation over $e$ indicates the usual element assembly process.

In order to avoid singularities in the numerical implementation, the first term in the stiffness interpolation, $\lambda_E \varphi_e^p$, is replaced with $\lambda_{E,min} + (\lambda_E - \lambda_{E,min})\varphi_e^p$. This ensures a strictly positive minimum stiffness ($\lambda_{E,min} E^0$).

### *2.4. Influence of base structure feature size on coating thickness*

As already pointed out, the uniform coating thickness relation (8) only holds if the given feature in the base structure is sufficiently wide compared to the coating thickness. In Figure 4a, a sequence of 1D plots with decreasing feature size is shown to illustrate this point. The width, $w$ indicates the width of a sharp-edged feature in the design variable field, $\mu$. The resulting filtered and interpolated fields are obtained using the parameters $R_1 = 10.0$, $t_{\text{ref}} = 1.0$, $\eta = 0.5$ and $\beta = 64$, i.e. the same choice as for the MBB beam benchmark study which will be presented in Section 4.1.

The top plot of Figure 4a shows the case of $w > R_1$. Here the base structure feature defined by $\varphi = \bar{\tilde{\mu}}$ is coincident with the design field feature. The base structure feature width may be defined as being delimited by the points where $\varphi = \eta = 0.5$. In the subsequent plots, $w < R_1$ and the base structure feature becomes smaller than the design field feature, an effect which accelerates with decreasing feature size. Since a well-defined coating requires a well-defined feature in the base structure, the modeled coating thickness decreases when the base feature becomes too thin. This effect accelerates in parallel to the decreasing base structure feature size.

In Figure 4b the modeled coating thickness, $t$, is plotted as a function of the feature size for the six 1D cases in Figure 4a. The dashed line with circle markers plots $t(w)$, i.e. $t$ as a function of the feature width in the design field. To illustrate the connection to the feature size in the base structure, also $t(\bar{w})$ is plotted, i.e. $t$ as a function of the resulting base structure feature size (dotted curve with square markers). Take as example the fourth 1D plot, where a design feature of $w = 4.4$ results in a base structure feature of width $\bar{w} = 2.17$. The resulting coating thickness of $t = 0.87$ is plotted as a function of both these numbers.

Figure 4 reveals the behavior of the interpolation function when the feature size goes towards zero. An ideal model would impose a constant coating thickness for any feature of non-zero width. If assuming a coating-based manufacturing method, the model should not permit a double coating layer without base structure, while an additive manufacturing-oriented model should be fully free to merge the two shells. However, with the interpolation function used in this work the coating vanishes before the base structure feature reaches a width close to zero.

For the filter parameters used for the plots in Figure 4 even a base structure feature as small as $\bar{w} = 2.17$ will be modeled with 87% of the reference coating thickness. At the plot for $w = 5$ the base structure feature is $\bar{w} = 3.5$ wide and the coating has the full thickness of 1.0. In other words, only very small features cause issues with the modeled coating thickness. For the optimizations performed in this paper, no issues were observed. However, if the issue appears, it can be alleviated by including feature size control for the base structure. Possible formulations for this aim include the robust formulation (Wang et al., 2011) or explicit constraints (Zhou et al., 2015). This extension is left for future studies.

### *2.5. Sensitivity calculation*

Due to the form of the interpolation function for stiffness and density, the sensitivity analysis for the coating problem involves several chain rule derivations. The reader is referred to Clausen

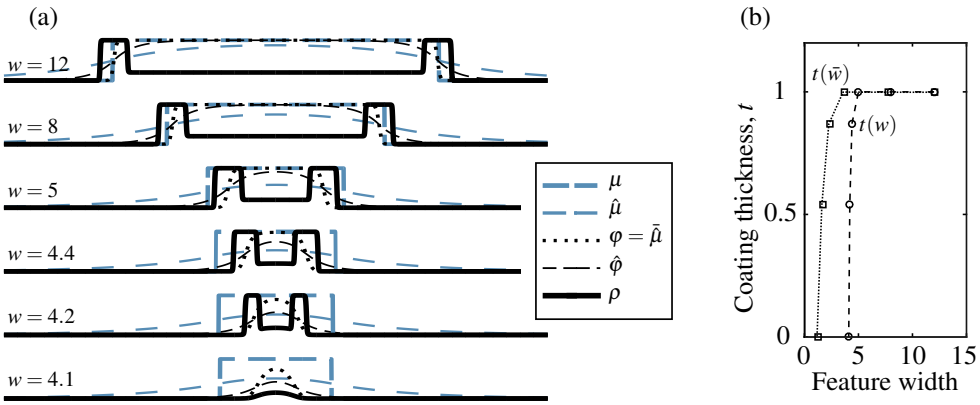


Figure 4: Dependency of physical density interpolation function on feature width, $w$, in the underlying field of mathematical design variables, $\mu$. (a) Sequence of sharp-edged features of varying thickness in the design field and the resulting physical density interpolation. (b) Modeled coating thickness, $t$, as a function of the feature width, $w$.

et al. (2015) for details. Design updates are performed using the method of moving asymptotes, MMA (Svanberg (1987)).

## 3. Implementation

This section describes considerations for the choice of boundary conditions (BCs) used for the PDE-filters. Since the material interpolation function depends both on the design field and its gradient, the choice of filter BCs is non-trivial. We employ the domain extension approach (Clausen and Andreassen, 2017) in order to eliminate boundary effects from the density filters. The idea is explained in more detail in the following and sketched in Figure 5a.

The first filtering step must ensure a base structure with crisply defined structural edges, not only in the interior of the domain, but also in the vicinity of the design domain boundary. Consider a sharp feature in the design variable field, $\mu$. Figure 5a shows such a feature, indicated by a dashed, bold, blue line. The feature is located at the domain boundary. When applying the first density filter, the feature will be smoothed anti-symmetrically around the domain boundary (dashed, thinner blue line). Assuming a feature of sufficient width, the edge of the base structure (dotted black line) will be coincident with the edge of the feature in the design variable field, since the threshold of the first projection is $\eta = 0.5$. Subsequently, the coating will occupy half a thickness on each side of the edge. Hence, the base structure—and consequently the domain of mathematical design variables, $\mu$—cannot extend closer than $t_{\text{ref}}/2$ from the domain border of the physical design domain, if space should be left for the coating.

Following the domain extension approach (Clausen and Andreassen, 2017), the smoothing of the design field (6) is performed with a void padding extending at least one filter radius from the design domain boundary, as this will eliminate edge effects. If the domain extension is performed with a sufficiently wide padding, it will make no difference whether homogeneous Neumann or homogeneous Dirichlet BCs are used in this smoothing step. Here we employ homogeneous Neumann BCs, as its implementation is trivial.

For the second filtering step which enforces the coating, the domain extension from the first step is reused. This eliminates further boundary effects.

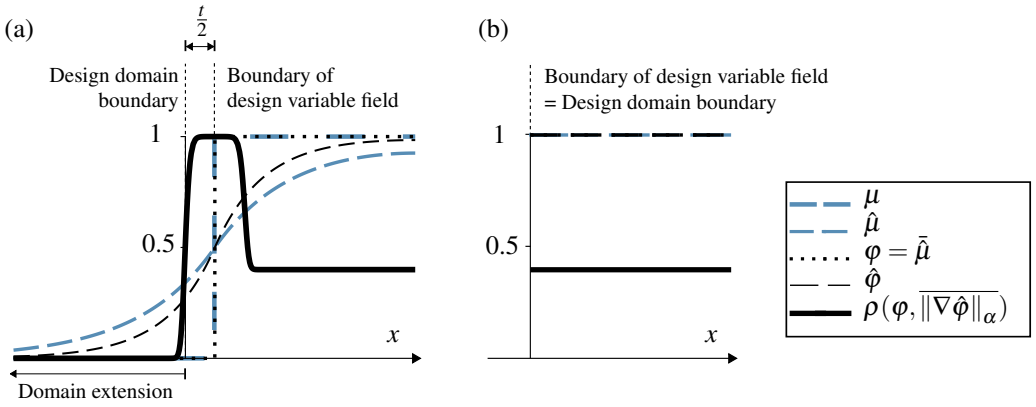


Figure 5: Coating interpolation function at design domain boundary for a sharp feature which lies exactly at the design variable field boundary (1D example). Points left of the design domain boundary are outside the domain. (a) Domain extension approach ensures correct coating at boundary. (b) Homogeneous Neumann BCs in both filtering steps permit omission of coating. In the example the fields $\mu$, $\hat{\mu}$, $\varphi$ and $\hat{\varphi}$ all equal 1.

At loads and supports, a local modification is employed: The domain extension is omitted in the first smoothing, and instead homogeneous Neumann BCs are employed directly at the boundary of the field of mathematical design variables. This follows the suggestion from Clausen and Andreassen (2017). Since coating must be enforced also at loads and supports, the domain extension is not omitted in the second smoothing step.

Note, that at a symmetry condition, the domain extension is omitted and homogeneous Neumann BCs are chosen for both filtering steps, as this choice eliminates gradients and thereby implies that coating is avoided (Figure 5b).

## 4. Results

Three different test problems will be considered: the MBB beam benchmark problem, a T-bracket, and a branching design problem.

### *4.1. MBB beam*

First a 3D MBB beam benchmark problem is considered. For all porous structures, the infill is assumed to exactly attain the upper HS bound. In order to avoid thin, non-robust features in the fully solid structure, this structure is optimized using a filter radius equal to the porous base structure filter radius, $R_1$.

As a means for testing our hypothesis that porous structures are more robust towards load perturbations than fully solid structures, we will numerically test the optimized structures for an off center (asymmetric) load case, which is different from the load case they were optimized for. The load magnitude is identical to that used in the optimization, but now applied asymmetrically on only one half of the beam width, from the edge to the center.

Figure 6 shows the design domain, including loads and supports. The physical design domain is the central blue box, having a side length ratio of 3:1:1. Moreover, the domain extension used for the PDE-filters is shown (surrounding light gray box) along with dark gray boxes at loads and supports indicating where the filter domain is not extended. A single symmetry condition is used at the left end. The domain was discretized using $288 \times 96 \times 96$, or 2.7 million, tri-linear brick

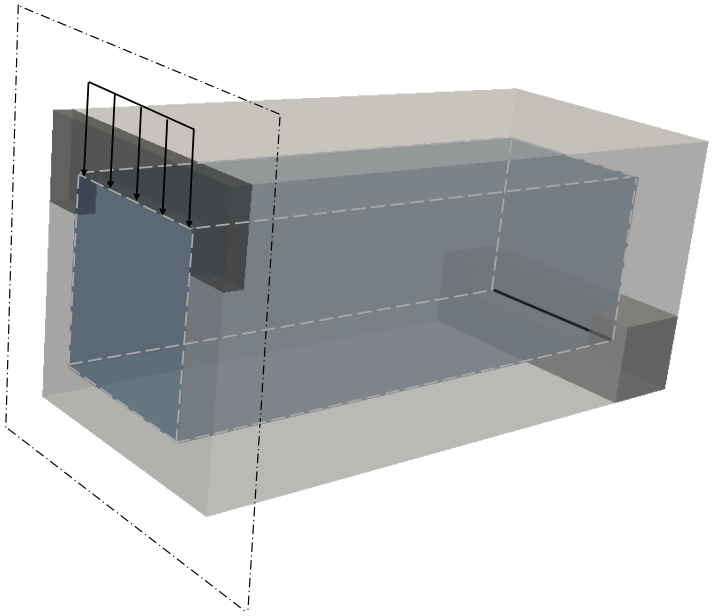

Figure 6: Design domain for MBB beam problem. The physical design domain is the central blue box indicated by dashed edges. The side length ratio is 3:1:1. The domain extension used for the PDE-filters is indicated by the surrounding light gray box. The load is applied vertically at the center line of elements, half a coating thickness from the top face. The black solid line is simply supported. It is located half a coating thickness from the domain borders. The dark gray boxes at loads and supports indicate where the filter domain is not extended, cf. Section 3. A single symmetry condition is used.

elements in order to be compatible with the employed multi-grid FE solver (the element number in each dimension was an integer multiple of 8). For simplicity, the dimensions of the domain were chosen such that the element side lengths were 0.5, that is, as $144 \times 48 \times 48$. The first filter radius was $R_1 = 10.0$ and the coating thickness was $t_{\text{ref}} = 1.0$. The maximum number of iterations was 600. The computations were run using 320 processes (16 nodes with 20 processes per node) with an average CPU-time of 794 hours (corresponding to a wall clock time of 2h29min) for the 25% volume fraction problem and 1869 hours (corresponding to a wall clock time of 5h51min) for the 10% volume fraction problem (without optimizing for computational speed).

We created two series of optimized structures at a volume constraint of 25% (Figure 7) and 10% (Figure 8), respectively. For each series a fully solid structure was used as a reference and compared with four porous structures with infill stiffnesses of 0.1, 0.2, 0.5 and 0.8, corresponding to infill densities of 0.18, 0.33, 0.67 and 0.89, respectively, assuming that the HS upper bound is attained, see Equation (1).

Figure 7 shows the five optimized structures for the 25% volume fraction, along with cross sections through the center point, normal to the $x$, $y$ and $z$ directions, respectively. For the visualization the coating elements and the base structure are thresholded individually at 0.5. The coating is defined by $\overline{\|\nabla\hat{\varphi}\|_\alpha}$, while the base structure is defined as $\max(\varphi - \overline{\|\nabla\hat{\varphi}\|_\alpha}, 0)$ to avoid overlapping elements.

The first three structures (solid, $\lambda_E = 0.8$ and $\lambda_E = 0.5$) have identical topology with a clearly defined I-beam-like shape to sustain the bending load. For the porous structure with $\lambda_E = 0.2$, the infill is sufficiently light so that two parallel I-beams can be created, thus better exploiting the stiffer coating material. The last structure, $\lambda_E = 0.1$, performs reasonably well but illustrates an issue which was also observed in the 2D problem (Clausen et al., 2015): if $\lambda_m$ is smaller than the volume fraction, the volume constraint is not active in the first iterations. The reason is that using a uniform initial guess for the design field implies that gradients are zero in the interior of the design domain. Without an active volume constraint, hole nucleation might fail to happen.

Figure 9a plots compliance values for the five structures (indicated by solid squares), normalized with respect to the fully solid structure. As was observed in the 2D problem, the compliance generally increases with smaller infill density due to the sublinear relation between density and stiffness given by the upper HS bound curve. However, the structure with $\lambda_m = 0.89$ performs as well as the fully solid structure. The five structures are furthermore evaluated for the off center load case (indicated by circles). For this load case all structures perform similarly, except for the structure with $\lambda_m = 0.33$ which performs 12% better than the fully solid structure. The lower the infill density, the smaller the relative decrease in performance due to the load perturbation.

The five optimized structures for the 10% volume fraction are presented in Figure 8. Here, a larger variation in the topologies is observed due to the more limited amount of material. For the fully solid structure, there is no longer enough material to generate a full, vertical plate. Instead, three holes are introduced, making the $y$ cross section more similar to the topologies which are typical for 2D problems. Still, an I-beam-like shape is observed in the $x$ cross section, however, the flanges are very narrow.

The next three structures, $\lambda_m = 0.89$, $\lambda_m = 0.67$ and $\lambda_m = 0.33$, have identical topology. The most important difference to the fully solid structure is that two holes have been closed, and the $y$ cross section is now predominantly a solid plate (the I-beam web). The flanges gradually become wider with lower infill density. For the last structure with $\lambda_m = 0.18$ the plate has been fully closed, and the flanges are wide and thin.

Note that the porous structures in this case suffer from small areas for which the coating is absent. This effect may be attributed to a too steep continuation scheme employed for the

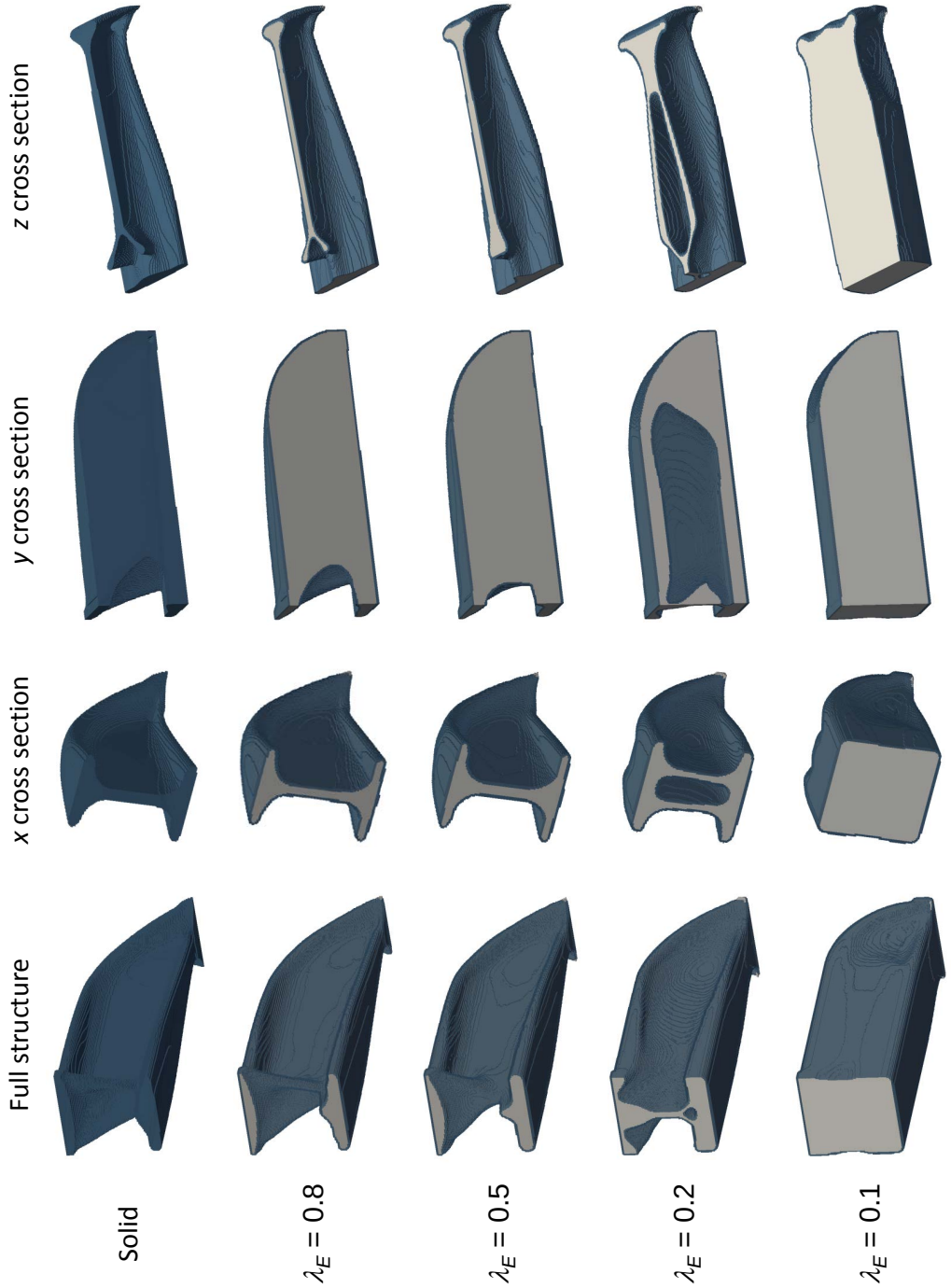


Figure 7: Optimized MBB beam structures for a volume constraint of 25%. From the top: Fully solid structure, then four porous structures. The infill stiffnesses of 0.8, 0.5, 0.2 and 0.1 correspond to infill densities of 0.89, 0.67, 0.33 and 0.18, respectively.

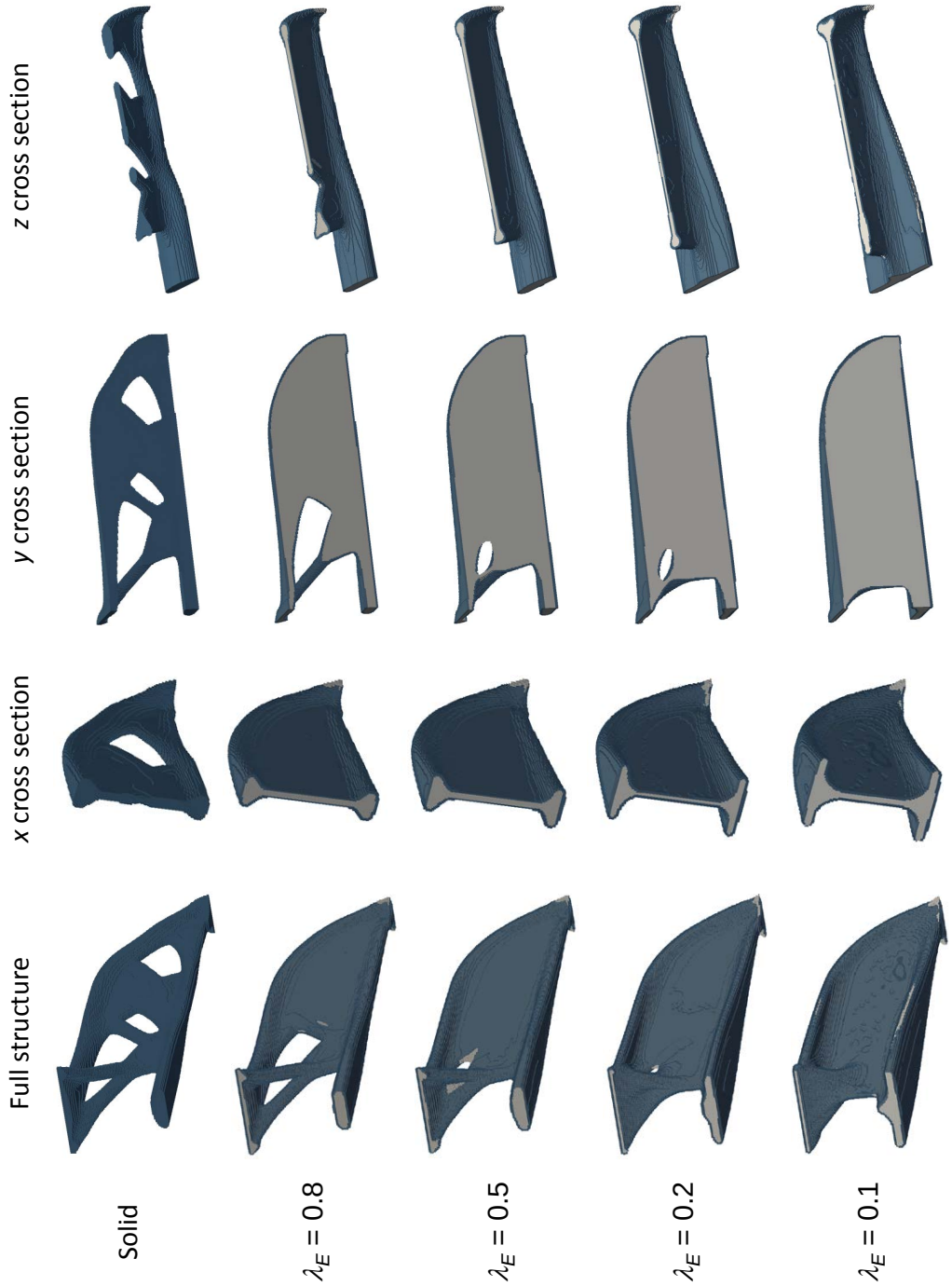


Figure 8: Optimized MBB beam structures for a volume constraint of 10%. From the top: Fully solid structure, then four porous structures. The infill stiffnesses of 0.8, 0.5, 0.2 and 0.1 correspond to infill densities of 0.89, 0.67, 0.33 and 0.18, respectively.

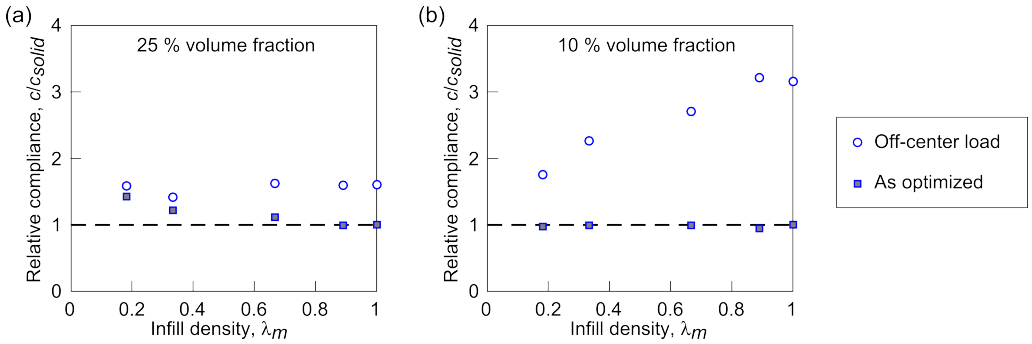


Figure 9: Comparison of the structural performance. Compliance values are normalized with respect to the fully solid structure. Solid squares indicate compliance when evaluated with the same load case as used in the optimization. Circles indicate compliance when evaluated with an off-center load of the same magnitude. (a) MBB beams of 25% volume fraction. (b) MBB beams of 10% volume fraction.

projection. A more slowly applied continuation might alleviate this issue.

Compliance values, again normalized with respect to the fully solid structure, are shown in Figure 9b. Here, the picture is somewhat different than for the 25% volume constraint case. All compliance values are more or less identical, despite the relatively softer infill material. In all cases the designs seem to pursue an I-beam-like shape, which is not surprising for the bending-dominated load case. There appears to be a trade-off between making a solid, vertical plate (the I-beam web) and ensuring wide flanges. The introduction of a porous interior permits ensuring both features simultaneously. This was not possible for the fully solid structure due to the filter radius, which is large compared to the coating thickness for the porous structures. This seems to be the reason for the similar performance in compliance. This observation fits well with the effects which have been observed in a recent study on the optimality of Michell structures (Sigmund et al., 2016).

Also these five structures were evaluated for the off center load case (indicated by circles). In this case, the three porous structures of lowest infill density perform remarkably better than the fully solid structure. The compliance of the porous structure with an infill density of $\lambda_m = 0.18$ is nearly 45% lower than for the fully solid structure.

Considering simultaneously the compliance plots for the two series of structures (Figure 9a-b), there is a clear trend that the porous structures are less sensitive towards the asymmetric load perturbation. The effect is more pronounced for the 10% volume constraint, where the material limit puts stronger restrictions on the designs. For the 25% case, the I-beam-like shape is well realized for all five designs, and the benefits of using porous material is smaller. The application of porous structures therefore appears to be most valuable for design problems subject to a low volume fraction constraint, since such designs generally are more sensitive to load perturbations and more prone to e.g. buckling failure.

### *4.2. T-bracket*

In addition to investigating the MBB beam example, we performed a similar study for a more complex example, a T-bracket design problem. Figure 10 shows the design domain for the problem. The figure indicates two forces which are aligned with the $x$ and $z$ directions, respectively. In order to test the optimized structures for load uncertainties, the optimization was

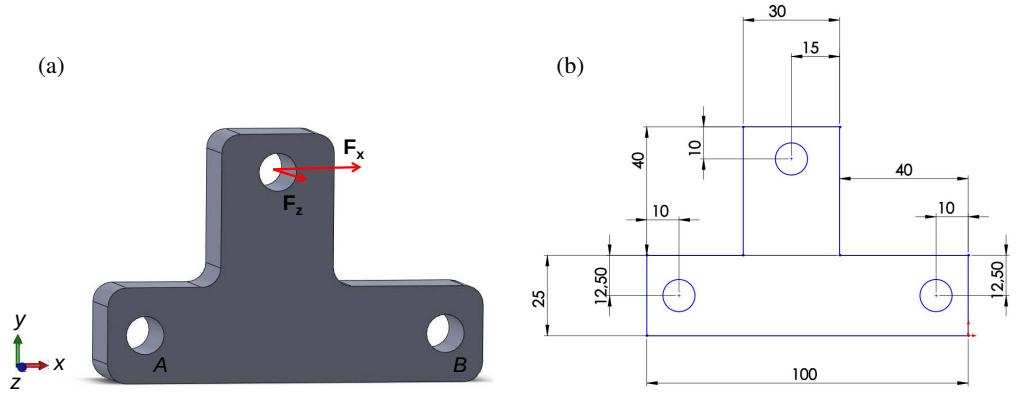


Figure 10: Design domain for T-bracket problem. (a) Full design domain. The part is clamped at the holes $A$ and $B$ (radius 5). The forces $\mathbf{F_x}$ and $\mathbf{F_z}$ are applied at the central point of the cylindrical hole (with radius 5) by means of a solid rod, and $F_x = F_z = 1$. (b) Part dimensions for an $xy$ cross section. The depth in the $z$ direction is 20. The fillets which are applied to all edges aligned with the $z$-axis (radius: 5) have been omitted in the cross-section figure for clarity.

run with a single load case in which the two forces were applied simultaneously. Afterwards, the optimized structures were evaluated both for the design load case and for the cases where the two forces were applied individually.

Since the MBB example indicated that the advantage of using porous structures is higher for low volume fractions and low infill density, we used a 10% volume constraint and only designed a single shell structure with $\lambda_E = 0.2$ and $\lambda_m = 0.33$ for comparison with a corresponding fully solid structure. The bounding box of the design domain was discretized using a regular grid of $400 \times 264 \times 104$ tri-linear brick elements. The total number of elements inside the design domain was 5.7 million, which also equals the number of design variables. The first filter radius was $R_1 = 3.0$ and the coating thickness was $t_{\text{ref}} = 0.5$. The maximum number of iterations was 600. The computations were run using 600 processes (30 nodes with 20 processes per node) with an average CPU-time of 3079 hours (corresponding to a wall clock time of 5h8min), again without optimizing for computational speed.

Figure 11 shows the optimized structures. The trends in the performance are similar to those observed for the MMB beam problem optimized at a 10% volume fraction: The compliance of the porous structure is very close to that of the solid structure (only 1% larger) if evaluating the structure using the design load. However, if the $x$ or $z$ components of the load are applied individually, the compliance of the porous structure is 17% and 8% lower, respectively, compared to the solid structure.

Considering the images of the optimized structures, the reason for this performance improvement appears again to be that the porous structure has more freedom to exploit the advantageous closed wall configurations within the limits of the available material and the indirectly imposed length scale.

### *4.3. Branching problem*

In some cases, it is a manufacturing requirement that the feature size is uniform. An example is when using a coating-based process. First a polymer base structure is fabricated, e.g. using an adequate additive method. Next, this base structure is coated e.g. using electroplating, upon

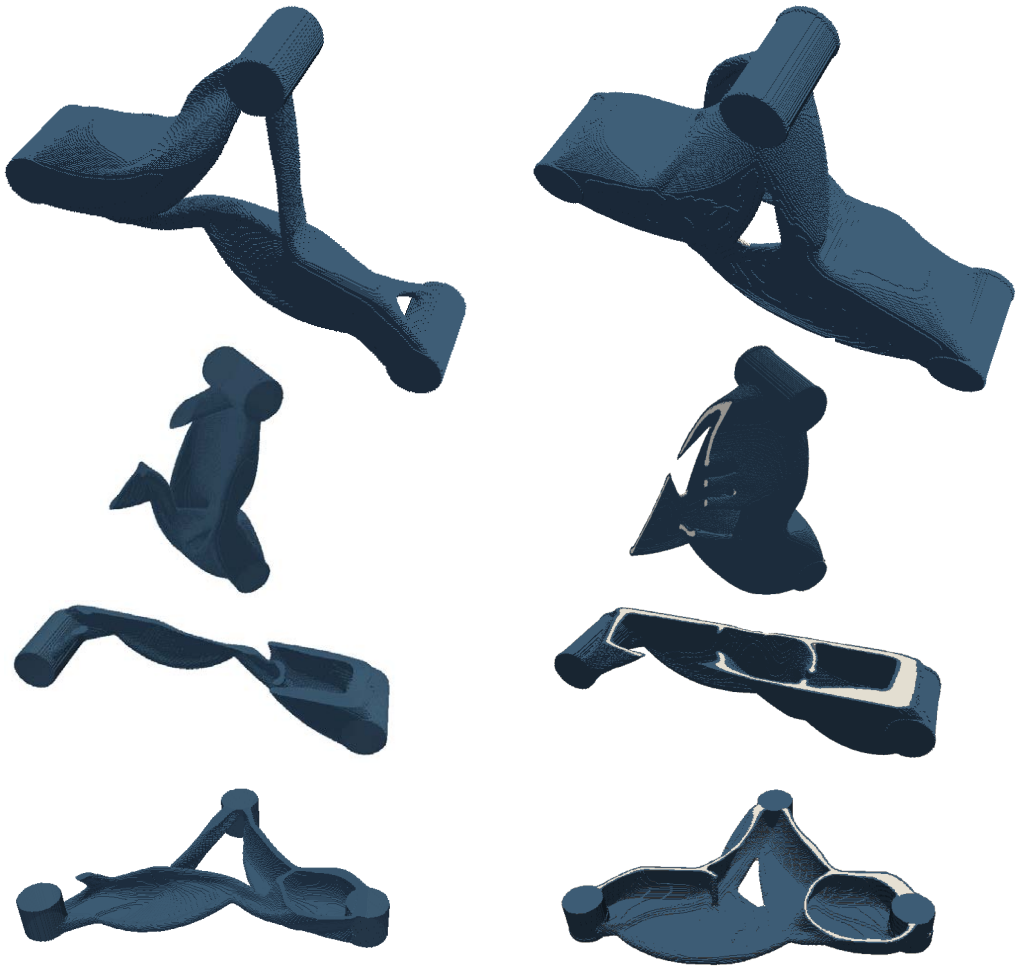

Figure 11: Optimized T-bracket components. Left: Solid structure. Right: Porous structure. From top: Full structure, and cuts with normal in the $x$, $y$ and $z$ directions, respectively.

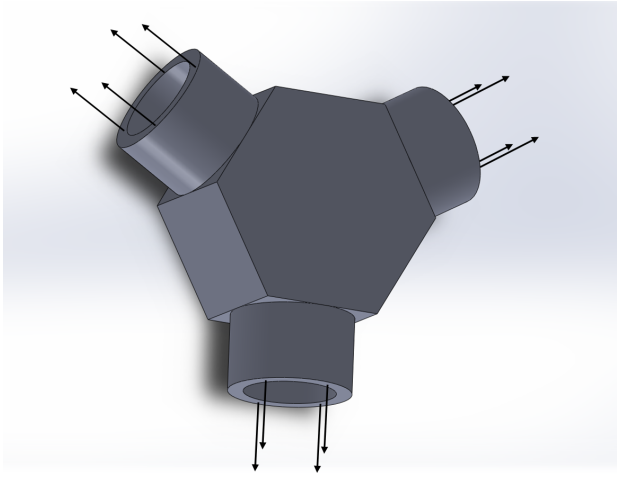

Figure 12: Design domain for branching problem. Forces balance exactly.

which the base structure may or may not be etched away (Schaedler et al., 2011). What remains is a hollow solid shell structure of uniform thickness. Such designs only make sense in 3D.

In order to explore this problem, consider Figure 12 illustrating a branching connection where three pipes meet. The three pipe sections are modeled as passive, solid domains with a passive void interior. The inner and outer radii are $r_i = 6$ and $r_o = 8$, respectively, and the pipe section length is $h = 10$. The design domain is the extruded, regular hexagon connecting the pipes as indicated in the figure. The side length and the extrusion depth of the domain are both equal to the outer diameter of the pipes, respectively $l_s = l_e = 2r_o = 16$. The pipes serve a load carrying purpose only, and only solid material should be used for the connection. In the considered load case, the pipes are all pulled away from the center point. Only a quarter of the domain is modeled, using two symmetry conditions. The forces balance exactly, so supports are only needed to make the numerical problem non-singular. Along with the symmetry FE boundary conditions, a single node at the edge of the hexagon at the midpoint between two pipes is clamped. As will be seen in the results, this node is located in a void part of the optimized structures. The problem is modeled in a rectangular cuboid FE domain of dimensions $25 \times 15 \times 50$ (accounting for symmetry). The $y$ direction is the extruded direction. The discretization used $56 \times 32 \times 104$ tri-linear brick elements. The computations were run using 80 processes (4 nodes with 20 processes per node) with an average CPU-time of 21 hours for 600 iterations (corresponding to a wall clock time of 16min).

By using a void infill, the coating method is also adequate for this type of shell design problem. In order to avoid numerical instabilities and a singular stiffness matrix, the void interior is modeled with $\lambda_E = \lambda_m = 10^{-3}$. The base structure radius is $R_1 = 8.0$ and the coating thickness is $t_{\text{ref}} = 1.9$, corresponding approximately to 4 element widths. The volume constraint is 30 %.

In order to have a benchmark for the result obtained with the coating approach, first two structures are created with a standard, solid optimization. The first case uses the base structure radius as the filter radius, $R = 8$, and the second case uses the coating thickness, $R = 1.9$. The resulting structures are shown in Figure 13a-b. The corresponding compliances are 215 and 205, respectively. In both cases the algorithm attempts to connect the pipe ends with a plate-like

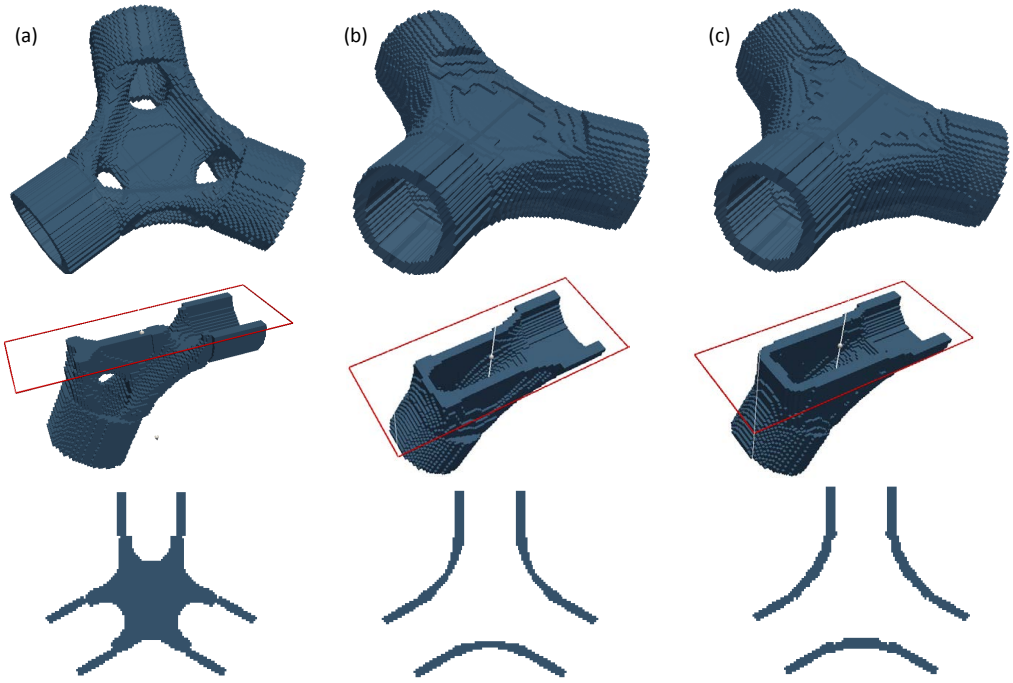


Figure 13: Optimized branching connection. From the top down: Full structure; cut at $x = 0$; slice at $y = 0$. (a) Standard solid with $R = 8$. $c = 215$. (b) Standard solid with $R = 1.9$. $c = 205$. (c) Coating approach with $R_1 = 8$, $t_{\text{ref}} = 1.9$ and $\lambda_m = \lambda_E = 10^{-3}$. $c = 206$.

structure. This prevents the generation of wide, thick features, even when using a large filter. The large filter does, however, enforce restrictions on the design and prevents the shell-like structure to be generated as is the case for the small filter, Figure 13b. Note however, that while the small filter results in a shell-like structure, the shell thickness is not uniform. This is best seen at the cut shown in the middle figure (the effect is not visible in the slice at the bottom). The shell has approximately double thickness at the corners in the cut and is thinner in the $y$ direction.

Now consider the structure obtained with the coating approach (Figure 13c). The structure has some resemblance with the structure in Figure 13b obtained with a small filter, however, the cut shown in the middle figure and the slice at the bottom reveals a constant coating thickness throughout the entire shell. The compliance is 206, that is, practically identical to the solid structure, which employs a small filter and has full design freedom. Clearly, a performance similar to that obtained with a free form approach cannot be expected for all design problems, since the uniform thickness requirement is a strong design restriction. This case again supports the validity of the coating approach for shell structure design problems.

## 5. Discussion

The numerical results support our initial hypothesis that porous shell structures are more robust towards load perturbations than fully solid structures. Both sets of MBB beam designs showed this tendency. However, for the high volume fraction (25%), the compliance of the

porous structures with respect to the load case they were optimized for was so much higher than for the solid structure that the "net gain" from introducing internal porosities is disputable. However, for lower volume fractions, porous structures become more relevant.

An effect that was seen in this 3D study which does not appear in 2D is the emergence of thin plates, both to support bending forces and in-plane, multi-axial loading conditions. Also for thin plates, porous structures are advantageous since they effectively act as sandwich structures. For the low volume fraction MBB beam study, the observed trade-off between a solid web (vertical plate) and wide flanges in the I-beam resulted in a solid structure which performed at the same level as the porous structures, but much more poorly resisted a load perturbation.

This improved robustness of porous infill structures adds to earlier results which indicate that porous structures have a higher buckling load. Again, something that is highly relevant for low volume fraction designs. An essential point is that both the robustness towards load perturbations and with respect to buckling are inherently ensured and are not explicitly included in the optimization. This is an important advantage since especially the buckling load is challenging and expensive to include as a design constraint.

The coating approach may in some cases provide a length scale advantage compared to fully solid structures. This both goes with respect to manufacturing, where coating can be applied in very thin layers, and with respect to structural performance, where the porous infill permits obtaining more robust structures with only a thin solid shell, as shown above. This effect is expected to partially explain that all MBB beams performed identically for the low volume fraction case. A fully solid structure should always have a better compliance compared to a porous structure, if it is allowed a sufficiently small length scale. This was confirmed in the pipe branching example.

A drawback of the coating approach is that a relatively fine resolution is required if a thin coating thickness is to be modeled. This is a consequence of using continuum elements for the modeling. For pre-defined topologies, other element types might provide better precision at lower resolution.

## 6. Conclusions

It has been shown that the coating approach, which previously only has appeared in a 2D implementation, is fully working in 3D. The addition of an extra dimension revealed new effects such as the appearance of thin plates and the possibility for creating pure shell structures of uniform thickness with a void interior.

The MBB beam and T-bracket results confirmed our initial hypothesis that porous shell structures have a significantly better robustness towards load perturbations than fully solid structures optimized under the same conditions. This observation mainly holds for lower volume fractions, where a porous shell structure can obtain topological advantages, such as closed wall configurations, due to the larger available volume.

For future research it will be relevant to validate these numerical results experimentally, including studies on infill performance for the 3D case for various manufacturing methods, and testing optimized structures both for load uncertainties and buckling.

## Acknowledgments

The authors acknowledge financial support from the Villum Foundation (the NextTop project) and DTU Mechanical Engineering.

## References


Aage, N., Andreassen, E., Lazarov, B. S., 2015. Topology optimization using PETSc: An easy-to-use, fully parallel, open source topology optimization framework. Structural and Multidisciplinary Optimization 51 (3), 565–572.

Andreassen, E., Lazarov, B. S., Sigmund, O., 2014. Design of manufacturable 3d extremal elastic microstructure. Mechanics of Materials 69 (1), 1–10.

Clausen, A., Aage, N., Sigmund, O., 2015. Topology optimization of coated structures and material interface problems. Computer Methods in Applied Mechanics and Engineering 290, 524–541.

Clausen, A., Aage, N., Sigmund, O., 2016. Exploiting additive manufacturing infill in topology optimization for improved buckling load. Engineering 2 (2), 250–257.

Clausen, A., Andreassen, E., 2017. On filter boundary conditions in topology optimization. Accepted for publication in Structural and Multidisciplinary Optimization.

Donoso, A., Sigmund, O., 2016. Topology optimization of piezo modal transducers with null-polarity phases. Structural and Multidisciplinary Optimization 53 (2), 193–203.

Guest, J., Prevost, J., Belytschko, T., 2004. Achieving minimum length scale in topology optimization using nodal design variables and projection functions. International Journal for Numerical Methods in Engineering 61 (2), 238–254.

Hashin, Z., Shtrikman, S., 1963. A variational approach to the theory of the elastic behaviour of multiphase materials. Journal of the Mechanics and Physics of Solids 11 (2), 127–140.

Lazarov, B. S., Sigmund, O., 2011. Filters in topology optimization based on helmholtz-type differential equations. International Journal for Numerical Methods in Engineering 86 (6), 765–781.

Møller, P., Nielsen, L., 2013. Advanced Surface Technology. Vol. 1-2. Møller & Nielsen.

Schaedler, T., Jacobsen, A., Torrents, A., Sorensen, A., Lian, J., Greer, J., Valdevit, L., Carter, W., 2011. Ultralight metallic microlattices. Science 334 (6058), 962–965.

Sigmund, O., 2007. Morphology-based black and white filters for topology optimization. Structural and Multidisciplinary Optimization 33 (4-5), 401–424.

Sigmund, O., Aage, N., Andreassen, E., 2016. On the (non-)optimality of michell structures. Structural and Multidisciplinary Optimization 54 (2), 361–373.

Svanberg, K., 1987. Method of moving asymptotes - a new method for structural optimization. International Journal for Numerical Methods in Engineering 24 (2), 359–373.

Torquato, S., Gibiansky, L., Silva, M., Gibson, L., 1998. Effective mechanical and transport properties of cellular solids. International Journal of Mechanical Sciences 40 (1), 71–82.

Vermaak, N., Michailidis, G., Parry, G., Estevez, R., Allaire, G., Bréchet, Y., 2014. Material interface effects on the topology optimization of multi-phase structures using a level set method. Structural and Multidisciplinary Optimization Published online, 1–22.

Wang, F., Lazarov, B. S., Sigmund, O., 2011. On projection methods, convergence and robust formulations in topology optimization. Structural and Multidisciplinary Optimization 43 (6), 767–784.

Xu, S., Cai, Y., Cheng, G., 2010. Volume preserving nonlinear density filter based on heaviside functions. Structural and Multidisciplinary Optimization 41 (4), 495–505.

Zhou, M., Lazarov, B. S., Wang, F., Sigmund, O., 2015. Minimum length scale in topology optimization by geometric constraints. Computer Methods in Applied Mechanics and Engineering 293, 266–282.